Impacts of Local Soil Moisture Anomalies on the Atmospheric Circulation and on Remote Surface Meteorological Fields during Boreal Summer: A Comprehensive Analysis over North America

Randal D. Koster

Global Modeling and Assimilation Office, NASA Goddard Space Flight Center, Greenbelt, Maryland

Yehui Chang

*Global Modeling and Assimilation Office, NASA Goddard Space Flight Center, Greenbelt, and
Goddard Earth Sciences Technology and Research, Morgan State University, Baltimore, Maryland*

Hailan Wang

*Global Modeling and Assimilation Office, NASA Goddard Space Flight Center, Greenbelt, and
Science Systems and Applications, Inc., Lanham, Maryland*

Siegfried D. Schubert

Global Modeling and Assimilation Office, NASA Goddard Space Flight Center, Greenbelt, Maryland

ABSTRACT

A series of stationary wave model (SWM) experiments are performed in which the boreal summer atmosphere is forced, over a number of locations in the continental United States, with an idealized diabatic heating anomaly that mimics the atmospheric heating associated with a dry land surface. For localized heating within a large portion of the continental interior, regardless of the specific location of this heating, the spatial pattern of the forced atmospheric circulation anomaly (in terms of 250-hPa eddy streamfunction) is largely the same: a high anomaly forms over west-central North America and a low anomaly forms to the east. In supplemental atmospheric general circulation model (AGCM) experiments, similar results are found; imposing soil moisture dryness in the AGCM in different locations within the U.S. interior tends to produce the aforementioned pattern, along with an associated near-surface warming and precipitation deficit in the center of the continent. The SWM-based and AGCM-based patterns generally agree with composites generated using reanalysis and precipitation gauge data. The AGCM experiments also suggest that dry anomalies imposed in the lower Mississippi River valley have remote surface impacts of particularly large spatial extent, and a region along the eastern half of the U.S.–Canadian border is particularly sensitive to dry anomalies in a number of remote areas. Overall, the SWM and AGCM experiments support the idea of a positive feedback loop operating over the continent: dry surface conditions in many interior locations lead to changes in atmospheric circulation that act to enhance further the overall dryness of the continental interior.

1. Introduction

From a societal perspective, much of what characterizes Earth's climate can be related to atmospheric processes: the mean and variability of rainfall in a region, for example, or the statistics of near-surface air temperature. The atmospheric component of climate, with its winds, storms, clouds, and aerosols, along with myriads of other processes, is overwhelmingly complex in and of itself. The full climate system, however, is made even more complex by the interactions of the atmosphere with the system's other components, notably the ocean, the land, and the cryosphere. The coupling of these different components allows, for example, the development and maintenance of modes of behavior,

Corresponding author address: Randal Koster, Global Modeling and Assimilation Office, Code 610.1, NASA/GSFC, Greenbelt, MD 20771.
E-mail: randal.d.koster@nasa.gov

such as the El Niño–Southern Oscillation (ENSO) phenomenon, that otherwise would not exist.

While the coupling of the different climate components increases the overall complexity of the system, it also has the beneficial impact of sometimes increasing climate predictability—the ability to predict ahead of time, perhaps weeks to seasons in advance, a climatic variation such as a regional drought. Atmospheric processes are strongly influenced by chaotic atmospheric dynamics. Because of chaos in the atmosphere, forecasts relying solely on atmospheric initialization cannot expect to have skill exceeding about two weeks. Time scales of variation in the ocean, land, and sea ice, however, and of various coupled modes such as ENSO, are much longer, and these longer time scales can translate, through coupling, to predictive skill for various atmospheric quantities. Operational seasonal forecasting systems indeed rely on the added predictability associated with the coupling of the atmosphere to slower components of the system (NRC 2010).

The coupling of the land to the atmosphere potentially allows the long time scales of soil moisture anomalies (from weeks to months; Entin et al. 2000; Vinnikov and Yeserkepova 1991) and snow anomalies (winter through the spring melt season) to contribute to atmospheric predictability at these time scales. The idea is simple—if a soil moisture anomaly, for example, is known at the start of a forecast, it can be predicted with some skill weeks to months into the forecast because of the slow time scale over which it varies. If weeks or months into the forecast the atmosphere in turn responds in a predictable way to the predicted soil moisture anomaly, then some skill is imparted to atmospheric prediction at these leads. The impacts of soil moisture variations on atmospheric variability have been studied extensively using both climate model analyses (e.g., Delworth and Manabe 1989; Douville and Chauvin 2000; Koster et al. 2006; Guo et al. 2006; Dirmeyer et al. 2013) and observational analyses (e.g., Betts and Ball 1995; Findell and Eltahir 1997; Koster et al. 2003; Taylor et al. 2011). Positive impacts of realistic soil moisture initialization on precipitation and air temperature forecast skill at monthly leads were quantified across a broad range of forecasting systems in the Global Land–Atmosphere Coupling Experiment, phase 2 (Koster et al. 2011). An impact of snow initialization on forecast skill was demonstrated by Peings et al. (2011) and Thomas et al. (2015).

The present paper focuses specifically on soil moisture anomalies, their impacts on the overlying atmosphere, and their associated impacts on remote precipitation and air temperature fields. The physical mechanisms underlying these impacts are not fully known. A local effect on the air temperature is straightforward; higher soil moisture levels can lead to increased evapotranspiration, which in turn leads to increased evaporative cooling of the land surface and, consequently, of the overlying air (Seneviratne et al. 2010). A local impact on precipitation can also be envisioned: higher soil moistures can increase evapotranspiration and accordingly reduce surface sensible heat flux, leading to a modification of the planetary boundary layer and thus to a modification of conditions determining the onset of moist convection (Betts et al. 1994). To what extent, however, can a soil moisture anomaly affect meteorological conditions in remote locations? On this subject the literature is more limited. For such a remote impact to be predictable—for information at the site of the soil moisture anomaly to be translated to the remote region—atmospheric transports or the atmospheric circulation itself would need to be modified in a predictable way. Douville (2002) suggested that certain soil moisture anomalies may help trigger stationary planetary waves over Europe that in turn may affect the transport of dry air from midlatitudes to the tropics. Lau and Kim (2012) connected extreme weather events in Russia and Pakistan through atmospheric patterns that were potentially amplified by dry land conditions. Koster et al. (2014) showed that forcing an atmospheric general circulation model (AGCM) with a soil moisture dipole over the continental United States—wet conditions in the Pacific Northwest and dry conditions in the southern Great Plains—leads to a distinct planetary wave pattern that induces further drying and warming in the latter region. Taylor et al. (2011) demonstrate the impact of surface moisture heterogeneity on the formation of mesoscale circulations that promote storm formation over dry regions. It is worth noting that the impacts of other land surface anomalies on the atmospheric circulation and associated remote impacts have also been examined; both Robock et al. (2003) and Cohen et al. (2014), for example, examined the role of Siberian snow cover on the atmospheric circulation and the associated potential for prediction, and Xue et al. (2012) examined the ability of subsurface soil temperature anomalies in the western United States to affect conditions in the eastern United States via Rossby waves.

In the present paper we expand on the findings of Koster et al. (2014) through a more comprehensive analysis of the impacts of North American soil moisture anomalies on the overlying atmospheric circulation and remote meteorological variables, with a focus on boreal summer. Results are shown in the order of the complexity of the models used to produce them. That is, after describing the models and the datasets examined (section 2), we first show a set of results (section 3a)

obtained by forcing a relatively simple stationary wave model (SWM) with an idealized heating anomaly that mimics the direct effect of surface drying. The SWM results have the advantage of demonstrating clearly one of our main findings, namely, that the atmospheric circulation responds in a similar way to heating anomalies imposed in very different locations. The SWM results, of course, also have the disadvantage of lacking physical processes and hence the physical complexities of a full AGCM; our second set of results (section 3b) is therefore obtained with a full suite of corresponding AGCM experiments. The AGCM results support the aforementioned main finding, although with the expected increase in noise and with added nuances in the patterns produced. The AGCM experiments also provide information on remote precipitation and air temperature impacts. We then examine available observations-based data (section 3c) and show that they in turn provide support for the SWM and AGCM findings. We conclude (section 3d) with supplemental analyses of the AGCM data that illustrate how the strength of soil moisture–meteorology teleconnections may vary in space.

Our AGCM analysis, by the way, utilizes large ensembles (~100–200 members), a reflection of the subtlety of the signals we seek here. We are, in effect, seeking the net impact (e.g., on mean states) of shifts in the probability density functions of various quantities rather than more deterministic relationships that would necessarily lead to a first-order improvement in predictions. This caveat should be kept in mind when evaluating the analyses that follow.

2. Models and datasets used

a. Stationary wave model

The nonlinear and time-dependent SWM used in this study is based on three-dimensional primitive equations in sigma coordinates. All of the basic variables in the model are deviations from a prescribed zonal mean or 3D climatological flow. The basic prognostic equations are those for perturbation vorticity, divergence, temperature, and the logarithm of surface pressure. The model-generated transient disturbances are suppressed by applying strong damping. The stationary wave solution is obtained by integrating the model to a quasi-steady state after a short period of time.

The model has rhomboidal truncation at wavenumber 30 (R30) in the horizontal and 14 unevenly spaced sigma levels in the vertical. While the R30 resolution (roughly 2.25° latitude × 3.75° longitude) is coarser than that of the AGCM described below (roughly 1° resolution), we nevertheless expect the AGCM and SWM results to be

directly comparable. This is because, relative to AGCM results, SWM results are not as affected by resolution. Much of the resolution-dependent behavior in an AGCM stems from its use of model physical parameterizations to produce stationary wave forcings such as diabatic heating. In contrast, diabatic heating in the SWM is prescribed and is thus not resolution dependent. Output from our R30 SWM experiments and that from SWM experiments at roughly 1° resolution should be similar.

The SWM has been shown to be a valuable tool for diagnosing the maintenance of the climatological atmospheric circulation and its anomalies (in terms of magnitude and pattern) as well as for investigating dynamics of stationary waves (e.g., Held et al. 2002; Schubert et al. 2011). See Ting and Yu (1998) for more details on the SWM.

b. Atmospheric general circulation model

The simulations examined here were performed with the Goddard Earth Observing System Model, version 5 (GEOS-5) AGCM, a component of the state-of-the-art modeling system maintained by the Global Modeling and Assimilation Office (GMAO) of the National Aeronautics and Space Administration's Goddard Space Flight Center (NASA GSFC). The version of the GEOS-5 AGCM used here is run on a cubed-sphere grid (Putman and Lin 2007). As is standard for this kind of system, unresolvable physical processes are parameterized; GEOS-5 uses the approaches of Moorthi and Suarez (1992) for convection, Bacmeister et al. (2006) for prognostic cloud cover, Chou and Suarez (1994) and Chou (1990, 1992) for longwave and shortwave radiation processes, Lock et al. (2000) for turbulence near the surface, and Helfand and Schubert (1995) for the surface layer (although over land the surface layer includes a viscous sublayer). Land surface processes are simulated with the Catchment land surface model (Koster et al. 2000), a model that simulates explicitly the impact of topography-driven subgrid soil moisture variability on the surface energy and water balances.

As with all AGCMs, the GEOS-5 AGCM has biases in its simulated climate. Nevertheless, the AGCM is well vetted. For the past several years, short-term weather forecasts produced by the model have been analyzed extensively by GMAO personnel every week to maintain confidence in model performance and to determine and correct deficiencies; this process ensures the continued maintenance of a state-of-the-art system. The AGCM has been deemed suitable for use in GMAO operations, serving, for example, as the model component of the Modern-Era Retrospective Analysis for Research and Applications reanalyses (MERRA and MERRA-2; Rienecker et al. 2011; Bosilovich et al. 2015)

and, when coupled to an ocean model, as the basis for GMAO seasonal forecasts (Ham et al. 2014). The GEOS-5 AGCM has been used extensively to study the mechanisms underlying climate variability (Schubert et al. 2014; Koster et al. 2014; Wang et al. 2016). Molod et al. (2012) document the performance (including biases) of the free-running model, and Gelaro et al. (2014) and Bosilovich et al. (2015) show, respectively, how the model behaves at very high resolution and within an analysis system.

c. Observations-based data

The SWM and AGCM simulations produce stream-function fields, and the AGCM also produces near-surface air temperatures and precipitation rates. To evaluate the realism of these model results, we interpret them in the context of available observations-based data.

We use reanalysis data to provide observations-based information on soil moisture, streamfunction, and near-surface air temperature. In the MERRA-2 reanalysis (Bosilovich et al. 2015), the land surface is forced with precipitation rates that are corrected with gauge-based precipitation observations (Reichle and Liu 2014). As a result, soil moisture contents in the MERRA-2 re-analysis evolve realistically, attaining the level of accuracy seen in traditional Land Data Assimilation System (LDAS) operational products (e.g., Xia et al. 2012). Note that because we utilize MERRA-2 root zone soil moistures only to determine periods for which the real world experienced dry land surface conditions, their level of accuracy should be acceptable; while the products of different LDAS systems do show differences, they nevertheless tend to be highly consistent in their identification of extreme dry periods (e.g., Koster et al. 2009; Wang et al. 2009).

We could also use MERRA-2 to provide the observations-based streamfunction and air temperature data we need, but we choose instead to extract these data from the European Centre for Medium-Range Weather Forecasts (ECMWF) interim reanalysis (ERA-Interim; Dee et al. 2011). This choice is driven by the fact that the AGCM experiments described below and the MERRA-2 reanalysis utilize the same atmospheric model, which could potentially promote similar biases in both sets of data. ERA-Interim provides observations-based data that are inherently more independent. [As it turns out, the use of MERRA-2 produces essentially the same results (not shown).] In addition, the near-surface air temperatures produced by ERA-Interim are known to be of high quality (Simmons et al. 2010), probably in part because ERA-Interim uses station measurements of air temperature to update soil temperatures.

For precipitation, we use the observations-corrected precipitation output from MERRA-2. Because we only look at precipitation totals for 10-day periods in June and July, the use of the observations-corrected MERRA-2 data is equivalent to using, over land, precipitation data from the Climate Prediction Center (CPC) Unified Gauge-based Analysis of Global Daily Precipitation (CPCU; ftp://ftp.cpc.ncep.noaa.gov/precip/CPC_UNI_PRCP/GAUGE_GLB/) database and, over the ocean, from a mix of data from the Global Precipitation Climatology Project (GPCP; Adler et al. 2003; Huffman et al. 2009) and the CPC Merged Analysis of Precipitation (CMAP; ftp://ftp.cpc.ncep.noaa.gov/precip/cmap/). In essence, then, we compare our AGCM precipitation results over land directly to rain gauge measurements. See Reichle and Liu (2014) for a description of how the different observational precipitation datasets were incorporated into the MERRA-2 data.

3. Experiments and results

a. SWM responses to idealized diabatic heating anomalies

In nature, a drier-than-average surface state (i.e., low soil moisture) can affect diabatic heating in the overlying atmosphere through its impact on the surface energy balance—the dry conditions lead to an anomalously high sensible heat flux from the surface and thus to increasing near-surface heating in the immediate area of the anomaly. When, in contrast, the surface is anomalously wet and latent heat flux dominates, the associated anomalous diabatic heating may appear geographically far away, depending on where that excess evaporated moisture eventually condenses.

To represent the immediate atmospheric impact of a dry surface anomaly and the associated local increase in sensible heat flux, we impose in the SWM, over a selected area of dryness, an idealized diabatic heating anomaly with the vertical profile shown in Fig. 1a. The areal extent of the imposed diabatic heating anomaly is given horizontal half-widths of 5° longitude and 5° latitude, as indicated in Fig. 1b for one of the experiments. This vertical distribution and spatial extent is consistent with the structures of the diabatic heating anomalies produced in the AGCM experiments described in section 3b below. To illustrate this, the vertical and spatial (zonal) structure of diabatic heating produced in a representative AGCM experiment (specifically, AGCM-L experiment, to be defined below) is illustrated in Fig. 1c.

In a standard experiment, the anomalous heating is imposed throughout the model integration. The mean basic state used for the SWM is the 3D June–July averaged
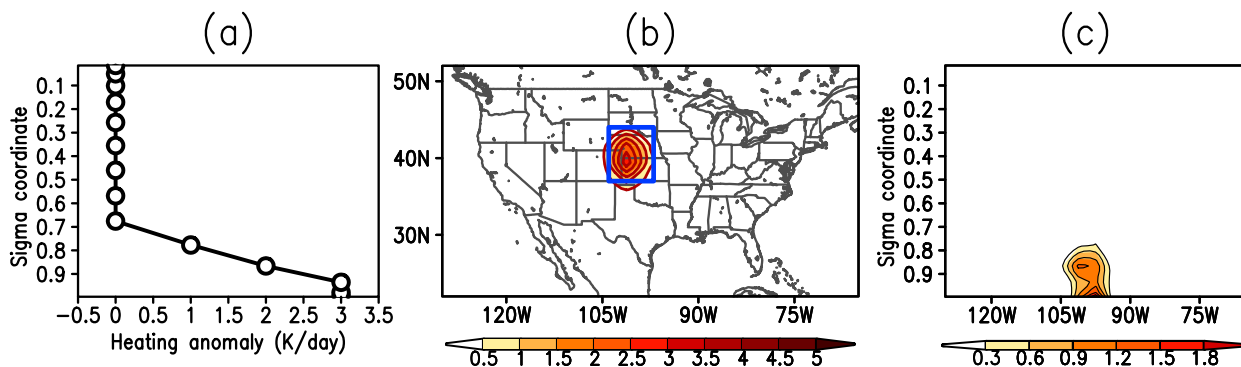
FIG. 1. (a) Vertical profile of idealized diabatic heating anomaly imposed in the SWM atmosphere over a selected geographical area. (b) Spatial distribution of imposed idealized heating anomaly (K day^{-1}) near the ground surface (model sigma level $\sigma = 0.9966$), for experiment SWM-L. (c) Vertical and zonal structure of the ensemble mean June–July diabatic heating anomalies (K day^{-1}) produced in experiment AGCM-L, averaged between 37° and 44°N.

climatological (1980–2010) basic flow taken from the GEOS-5 AGCM. The SWM reaches a steady state at about day 25, meaning that results from any day thereafter would represent the steady-state model response. Here we present the model eddy streamfunction solution at day 50.

We use this approach in a series of 21 experiments with the SWM, with each experiment assuming a different assumed area of dryness and thus a different geographical placement of the idealized anomaly shown in Fig. 1. Figure 2 shows the 21 geographical areas considered. In a given experiment, the imposed idealized anomalous diabatic heating was centered as close as possible (given the grid resolution of the SWM) to the central longitude and latitude of that experiment's indicated area. The 21 SWM experiments are hereafter labeled SWM-A through SWM-U.
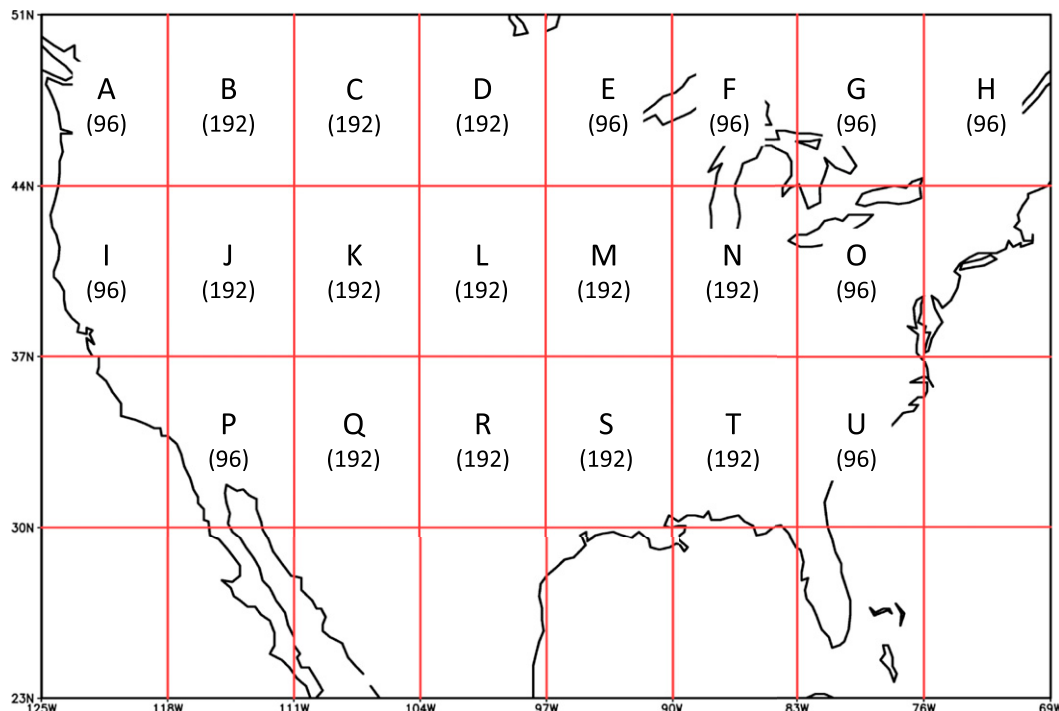

FIG. 2. Regions of imposed dryness considered in the 21 SWM and AGCM experiments (labeled A through U). In a given AGCM experiment, the indicated region was forced to be dry through the artificial zeroing of the incident precipitation in April through June. The number of AGCM ensemble members associated with each experiment is indicated in parentheses.

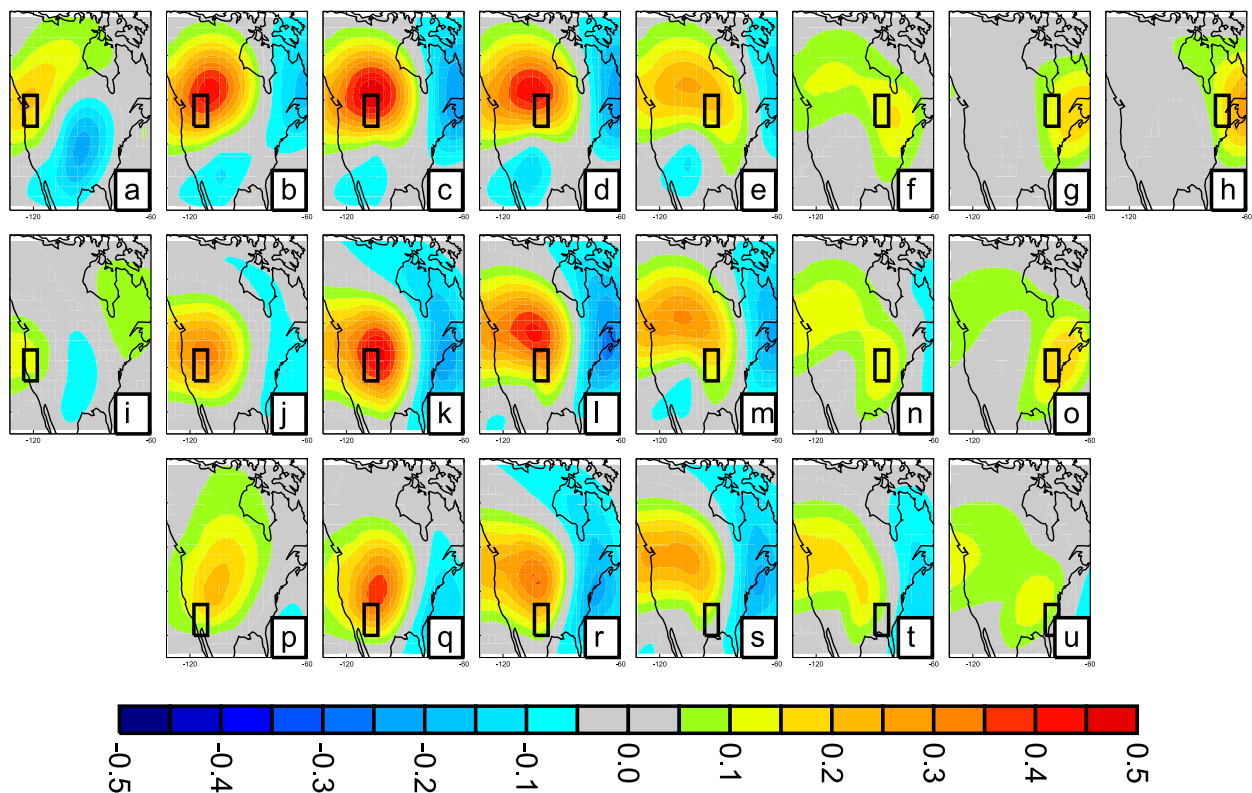## SWM Results: Eddy Streamfunction (10^6 m^2/s)

FIG. 3. Eddy streamfunction anomaly fields at 250 hPa produced in the SWM experiments. The boxes indicate the regions for which the idealized diabatic heating source is placed.

Figure 3 shows the response of the 250-hPa eddy streamfunction field to the imposed heating anomaly in each experiment. Notice the similarity in the responses. In almost all of the experiments, a high anomaly is seen in the west-central part of the northern half of the continent, and in most of the experiments a low anomaly is seen farther to the east. The eddy streamfunction patterns generally look very similar in their placement, although the magnitudes of the responses are substantially reduced when the diabatic heat source is placed on the western coast, and the patterns change when it is placed toward the eastern coast. Certainly within the continental interior, different placements of the heat source promote a common atmospheric circulation response, with the maximum and minimum of the streamfunction field not simply shifting laterally with the heat source.

We choose the following approach to characterize the degree of similarity among the responses. We first average the 21 streamfunction anomaly fields in Fig. 3 into a single field and then compute the square of the spatial correlation r^2 between each experiment's 250-hPa streamfunction anomaly field and this average field over the North American area shown. The thick dashed lines in Fig. 4a enclose the nine experiments for which this r^2 is at least 0.65 (i.e., for which the average field over the 21 experiments explains about two-thirds or more of the spatial variance of a given experiment's field). Figure 4b then presents the results of a second averaging exercise; it shows the results of averaging the 250-hPa streamfunction anomaly fields over the nine experiments indicated in Fig. 4a.

A comparison of the individual streamfunction anomaly fields in Fig. 3 with the pattern in Fig. 4b shows that this pattern is indeed a first-order representation of the SWM results for these nine experiments. This point is underlined by Fig. 4c, which shows the square of the correlation coefficient between each experiment's streamfunction anomaly field and the nine-experiment average in Fig. 4b. Each of the nine experiments focusing on heating within the delimited area produces a streamfunction field in strong agreement with the nine-experiment average, with r^2 values upward of 0.7.

There are presumably many ways to characterize similarity in experiment results. Based on the approach
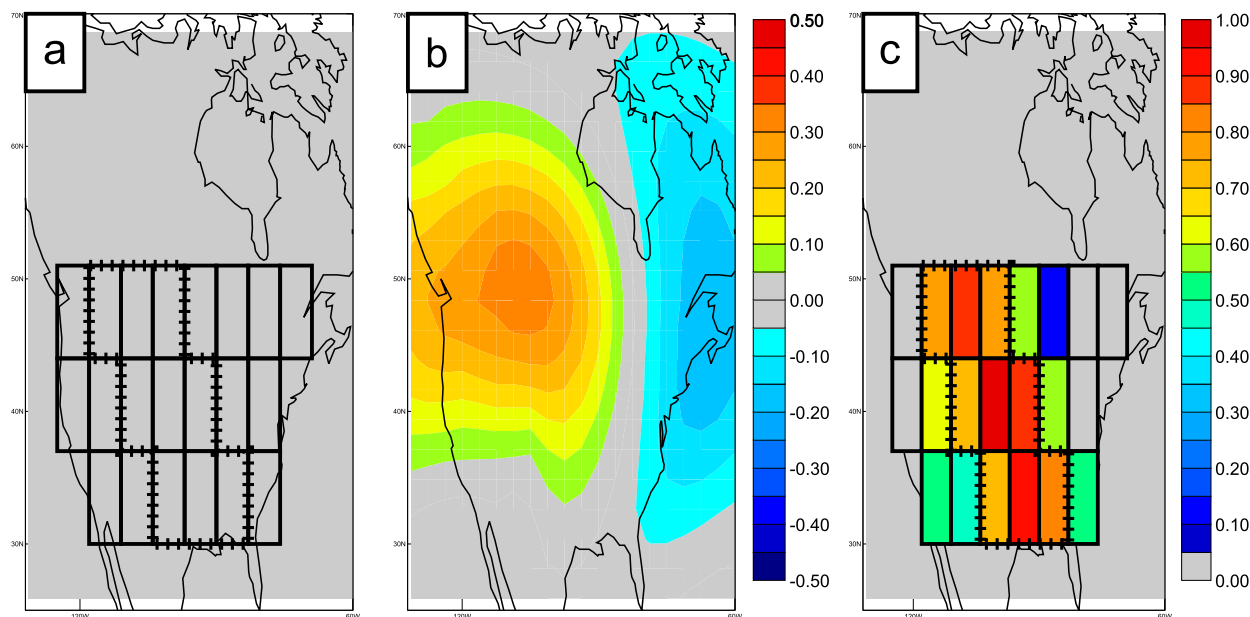
FIG. 4. Indication of the similarity between the 250-hPa eddy streamfunction responses in the different SWM experiments. (a) Location of the nine experimental regions for which the r^2 between the experiment's 250-hPa eddy streamfunction field and the average field over all 21 experiments over the North American area shown is 0.65 or higher (roughly two-thirds of variance explained by the averaged field). (b) Average of the computed 250-hPa eddy streamfunction fields ($10^6\,m^2\,s^{-1}$) over the nine experiments that examine heating within the region enclosed by thick dotted lines in (a). (c) The r^2 between each experiment's 250-hPa eddy streamfunction field (from the SWM analysis) and the nine-experiment average in (b). The value for a given experiment is shaded in color within the corresponding region in (c).

used here, we make the claim that the response of the 250-hPa streamfunction field to diabatic heating anywhere within the region delimited in Fig. 4a is similar in pattern—regardless of where surface heating is located in this region, the atmospheric circulation responds in much the same way. Much of our later analyses will focus on this interior region.

b. AGCM responses to imposed land surface dryness

The next step in our analysis is to determine if the basic pattern (Fig. 4b) found by the SWM for the interior region in Fig. 4a is also found within a full suite of AGCM experiments. We describe the AGCM experiments below.

1) CONTROL ENSEMBLE

The control for our experiments consists of an ensemble of 768 four-month simulations with the atmosphere and land components of GEOS-5. This decidedly large number of ensemble members helps ensure accurate statistics. Initialization followed the strategy employed by Koster et al. (2014): each simulation was initialized on 1 April 2012, with initial atmosphere and land conditions taken from different years of the MERRA reanalysis, and with the initial atmospheric conditions perturbed slightly to produce multiple ensemble members for each MERRA year. Sea surface temperatures for 2012 (a year for which the real world experienced warming

in the U.S. Great Plains) were prescribed using Atmospheric Model Intercomparison Project (AMIP)-style protocols (Gates 1992). Each simulation was performed on a C90 cubed-sphere grid (equivalent to $1° \times 1°$ resolution), and output from each simulation was subsequently written out onto a $1° \times 1°$ latitude–longitude grid for analysis.

2) EXPERIMENT ENSEMBLES

A total of 21 experiments were performed, each experiment consisting of an ensemble of either 96 or 192 simulations that differed from the control only in the prescribed drying of a selected land area. The drying of the selected area proceeded as follows. During every time step from 1 April to 30 June, any precipitation produced over the selected area by the AGCM was artificially zeroed before it reached the land surface, thereby allowing soil moistures in the land model there to evolve to levels corresponding to a 3-month dry period. The artificial zeroing of the precipitation ceased on 1 July, so that during the month of July, soil moistures were allowed to recover. The zeroing of the precipitation during 1 April–30 June was only at the surface; the AGCM's atmospheric vapor and temperature fields, having been modified by condensation processes in the production of precipitation, were not artificially reset to their prerainfall values.

The 21 areas considered in the AGCM experiments mimic those used for the SWM experiments (see Fig. 2), and we will thus refer to the AGCM experiments as AGCM-A through AGCM-U. The regions examined with the AGCM are, in fact, slightly smaller, an artifact of mapping issues associated with our use of a "cube grid" for the AGCM, a grid that does not translate exactly to a latitude–longitude grid. The areas, each roughly of size $7° \times 7°$, essentially span the continental United States. While the individual areas are somewhat smaller than the two examined by Koster et al. (2014), dryness anomalies within them are still able to affect the AGCM's overlying circulation, as will be shown later. The number of ensemble members comprising each experiment is listed in parentheses below the experiment identifier in Fig. 2.

As in the SWM analysis, experiment results relative to the control are analyzed for the period 1 June–31 July a time when land surface impacts on the atmosphere are expected to be large due to high surface turbulent fluxes. (We indeed expect land impacts to be reduced during fall through spring, when the turbulent fluxes are reduced due to reduced solar forcing.) In the context of the experimental design, the period examined corresponds to the final month of an extreme 3-month meteorological drought (June) and the first recovery month thereafter (July). Note that while a precipitation deficit was not imposed in the specified area during July, persistence ensured that soil moisture levels there during July remained significantly low. This is illustrated in Fig. 5a, which shows the percentile, based on the statistics of the control ensemble, of average July root zone soil moisture content produced by the experiments at each grid cell. The map is in fact a composite of results from the different experiments; percentiles shown within a given area are from the experiment that utilized that area. (High values along some edges, by the way, reflect the aforementioned slight inconsistency between the cube grid and a regular latitude–longitude grid.) July soil moistures tend to lie below the 5th percentile, indicating that soil moistures in the prescribed dryness regions, forced to be dry in June, do indeed remain dry through July. Deserts are an obvious exception, with the percentiles within region P in particular sometimes strongly (and surprisingly) exceeding 50%; note, however, that these regions feature a very small range of soil moisture in the control, with all control values at the very dry end. The high percentiles in region P are presumably artifacts, and the high values notwithstanding, July soil moistures in region P for experiment AGCM-P are themselves very low.

This last point is emphasized in Fig. 5b, which shows the difference in the total evaporation for June and July

between each experiment and the control. As in Fig. 5a, the map in Fig. 5b is a composite; results plotted within a given region are for the experiment focusing on that region (and indeed are derived, for this plot, from the first 96 ensemble members of the experiment). July evaporation rates from region P in experiment AGCM-P are not significantly increased, despite the percentiles shown for the region in Fig. 5a. More broadly, Fig. 5b is a useful reference because it indicates the relative strengths of the local diabatic heating anomaly effectively imposed in the different AGCM experiments, given the strong tie between evaporation and sensible heat flux. Whereas the SWM experiments imposed the same diabatic heating anomaly in the different regions, Fig. 5b shows that the effective strengths of these anomalies in the AGCM experiments varied across the country, with low values in the western and northeastern United States (e.g., in the neighborhood of the Great Lakes) and with higher values toward the southeast.

3) Basic results

Figure 6 shows the responses of the 250-hPa streamfunction, precipitation, and 2-m air temperature fields to the imposed dryness in region S in Fig. 2. (That is, the figure shows the difference between the mean fields for experiment AGCM-S and the corresponding mean fields for the control.) In Fig. 6, the solid lines, dashed lines, and thick white lines correspond respectively to differences that are significantly different from zero at the 95%, 99%, and 99.9% confidence levels, as determined by a Student's t test. Clearly seen in Fig. 6a is an induced wave pattern in the streamfunction difference field, with a high centered just to the north of the dry area, a low farther to the northeast, and another high even farther to the northeast, covering the south of Greenland. This wave pattern is clearly evident in the 2-m temperature difference field (Fig. 6c) and is also suggested in the precipitation difference field (Fig. 6b). In the particularly affected areas to the north and east of region S, precipitation is reduced by as much as $0.4\,\mathrm{mm\,day^{-1}}$, and temperature is increased by as much as 1 K—large differences given the 2-month averaging period. It is worth emphasizing here that, given the design of the experiment, the responses seen in Fig. 6 stem solely from localized soil moisture drying in the AGCM; the imposed soil moisture anomalies are indeed having an impact on the atmospheric circulation and on remote near-surface meteorology.

Results for all experiments are summarized in Figs. 7, 8, and 9. Figure 7 shows the full streamfunction anomalies induced by imposed dryness in the different areas. The anomaly patterns naturally vary among the experiments, far more than they do among the corresponding
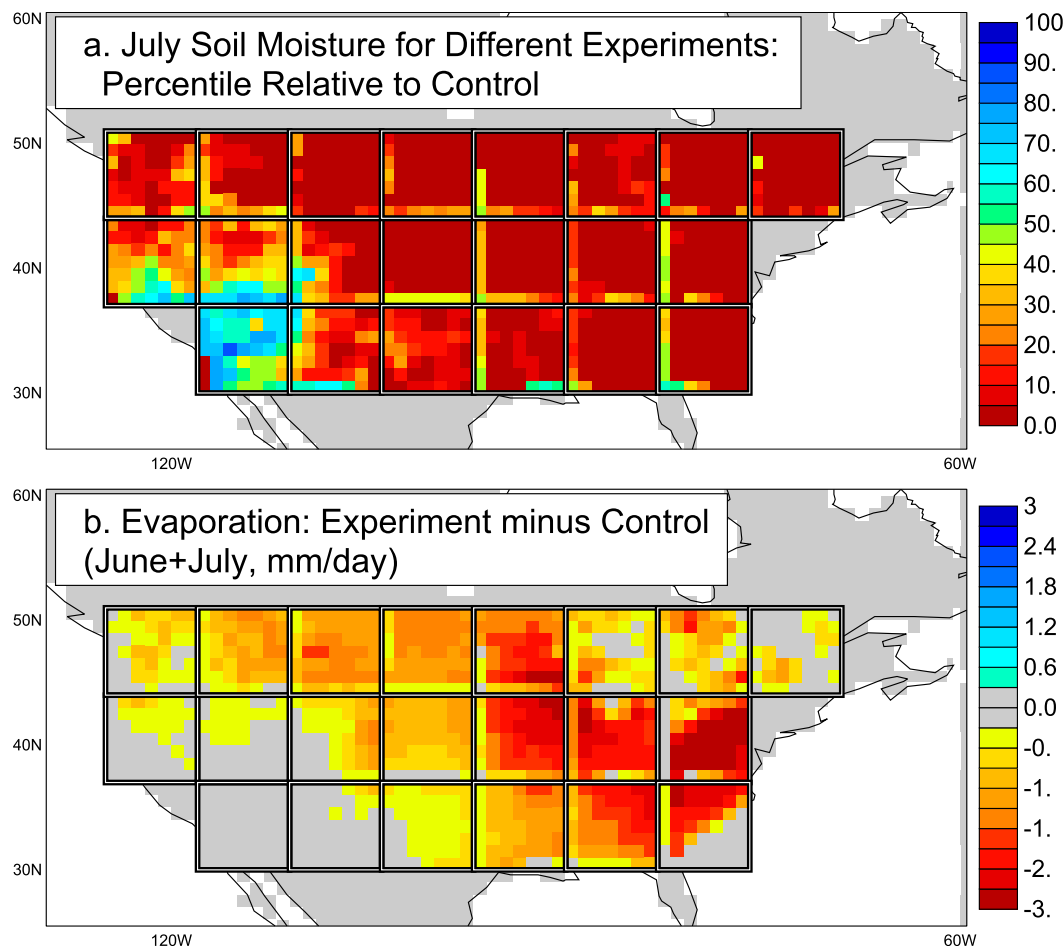
FIG. 5. (a) Percentile of average July soil moisture content in the different AGCM experiments, with rankings based on the full ensemble of control simulations. The percentile shown for a given grid cell is for the experiment in which that grid cell (along with its neighbors within the marked box) was forced to be dry during April through June; the map is thus a composite of results from different AGCM experiments. (b) Difference (experiment minus control) in the June–July evaporation computed in the AGCM experiments. The map shown in (b) is a composite as in (a), with the difference shown for a given grid cell being for the experiment in which that grid cell (along with its neighbors within the marked box) was forced to be dry during April through June.

SWM experiments. This is fully expected given the relative complexity of the AGCM. The differences between the SWM and AGCM experiments in their atmospheric circulation anomalies can be traced to their differences in stationary wave forcing anomalies. Relative to our SWM experiments, which utilize simple, localized diabatic heating anomalies (Fig. 1), the AGCM experiments produce more realistic diabatic heating anomalies that vary regionally, and they also (unlike the particular SWM experiments we performed) account for anomalies in transient flux convergences. In addition, unlike the deterministic SWM results, the AGCM results are affected by chaotic atmospheric dynamics, necessitating an averaging over a large number of ensemble members, and even with this averaging, sampling error still has some impact on the AGCM results.

Even so, the streamfunction anomalies produced in corresponding AGCM and SWM experiments do agree, at least to a first order. Notice, for example, that experiments SWM-F and AGCM-F both produce a similar swath of high values across southern Canada, and experiments SWM-O and AGCM-O both show that dryness on the far east coast locates the high positive streamfunction values relatively far to the east. While the patterns produced in experiments SWM-P and AGCM-P and in SWM-Q and AGCM-Q differ significantly, this difference can be traced to the fact that in the AGCM the zeroing of the rainfall in these regions did not lead to a large reduction in surface latent heat flux (and thus to a large increase in the heating of the overlying air through enhanced surface sensible heat flux), since soil moistures in the control simulations were
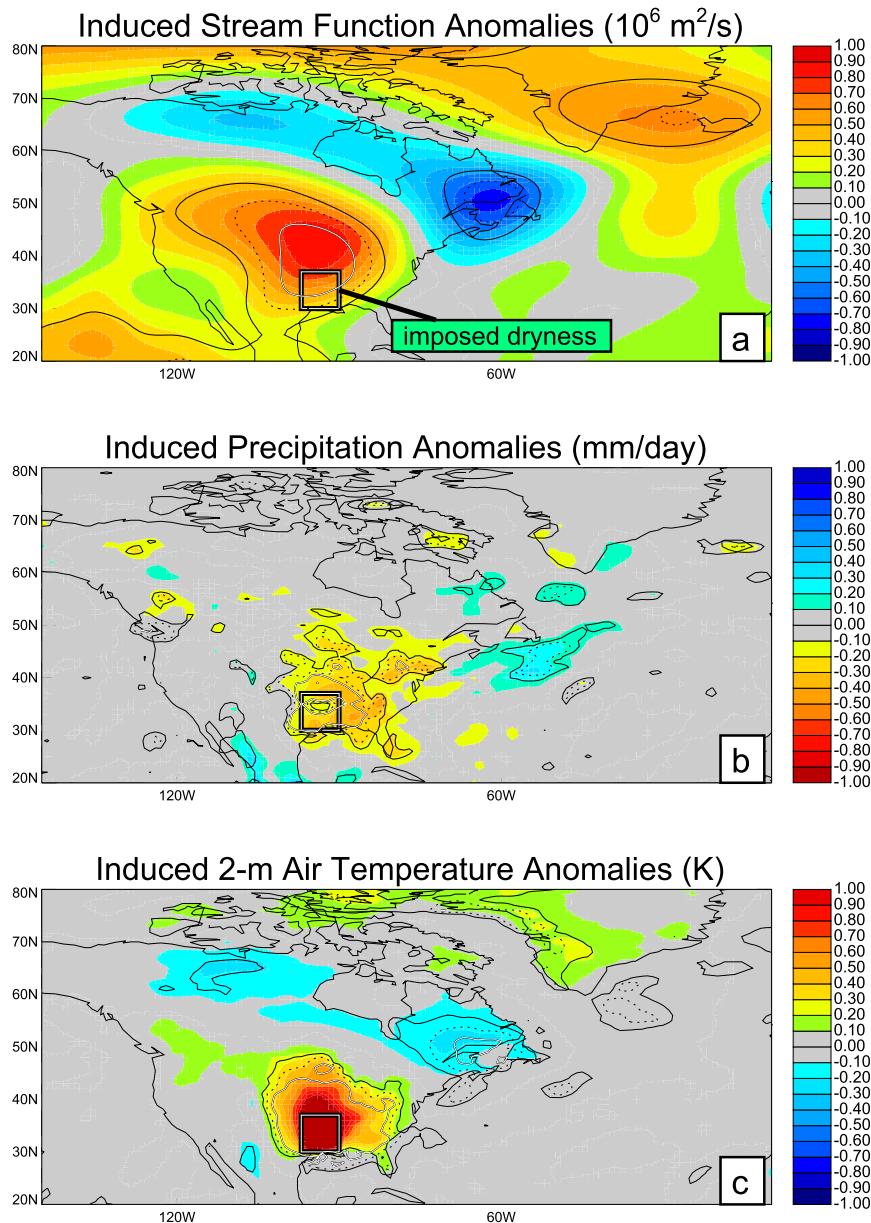
FIG. 6. (a) Anomalies (10^6 m^2 s^{-1}) in June–July 250-hPa streamfunction (experiment minus control) for experiment AGCM-S. The imposed dryness in region S has induced a wavelike pattern in the streamfunction field. (b) As in (a), but for June–July precipitation anomalies (mm day^{-1}). (c) As in (a), but for June–July 2-m air temperature anomalies (K).

already dry in these regions during the months considered (see Fig. 5b). The SWM and AGCM experiments were thus fundamentally different for both of these regions.

Consider now the experiments for which dryness is imposed within the area demarcated in Fig. 4a (AGCM-B, -C, -D, -K, -L, -M, -R, -S, and -T; the associated experimental results are enclosed within the red solid line in Fig. 7). An interesting feature seen for all of these experiments is the production of a high (with experiment-dependent magnitude) over the western-central United States and the corresponding production of a low that straddles the northeastern coast. Although the details differ (again, the AGCM is much more complex than the SWM, and the AGCM results shown here are affected somewhat by sampling), the basic first-order pattern produced by an imposed land surface dryness in the interior region is quite similar to that found for the

Induced Stream Function Anomalies (10^6 m^2/s)
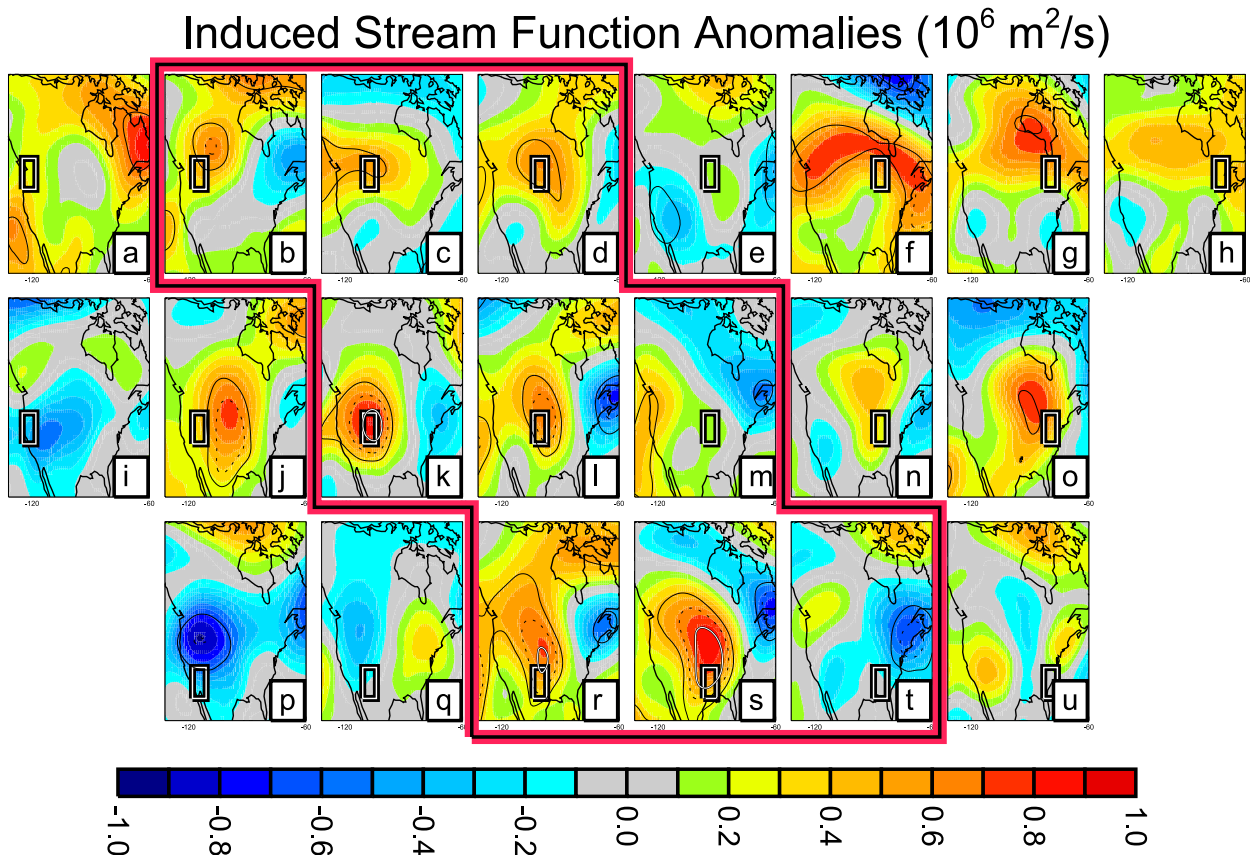
FIG. 7. (a) Anomalies in June–July 250-hPa streamfunction (experiment minus control) for experiment AGCM-A. Significance levels (according to a Student's t test) are shown as contours, with solid black for the 95% confidence level, dotted for the 99% confidence level, and solid white for the 99.9% confidence level. (b)–(u) As in (a), but for experiments AGCM-B–U. The thick red outline encloses the experiments corresponding to the continental interior region demarcated in Figs. 4a,c.

SWM. (This will be demonstrated further in section 3c below; averaging the precipitation changes produced by the AGCM experiments that focus on the demarcated interior region produces a field very similar to that shown in Fig. 4b for the SWM experiments.) In other words, the AGCM results support, certainly to a first order, the idea that dry conditions anywhere within the demarcated interior region produce a common atmospheric circulation response.

Beyond providing information on atmospheric circulation, the AGCM experiments are particularly interesting because they provide information on precipitation and near-surface air temperature response to the imposed dryness anomalies—they provide, in particular, some indication of how surface dryness can affect remote near-surface meteorology. Such remote impacts are examined further in section 3d. For now, consider Fig. 8, which shows the precipitation anomalies produced in the different AGCM experiments. To some degree, several of the experiments in the demarcated interior continental region produce similar precipitation reductions in

southern Canada and in the eastern half of the United States, down to the Gulf of Mexico (with details, of course, differing with experiment). Some similarities in precipitation response would indeed be expected from the aforementioned similar response in the streamfunction field, given that specific changes in large-scale atmospheric circulation can induce specific changes in precipitation.

Figure 9 shows the 2-m air temperature anomalies produced in the AGCM experiments. With a few exceptions (viz., regions I, J, P, and Q; desert regions for which the zeroing of precipitation did not strongly affect the soil moisture), the impact of the imposed drying is locally very strong, as might be expected given the associated reduced level of local evaporative cooling (Fig. 5b). Many experiments, however, show in addition a remote air temperature impact. Several of the experiments focusing on dryness in the demarcated region in Fig. 4a show warming along a swath extending from north-central North America to the Gulf of Mexico, a similarity that may stem from the aforementioned similarity in the streamfunction response.

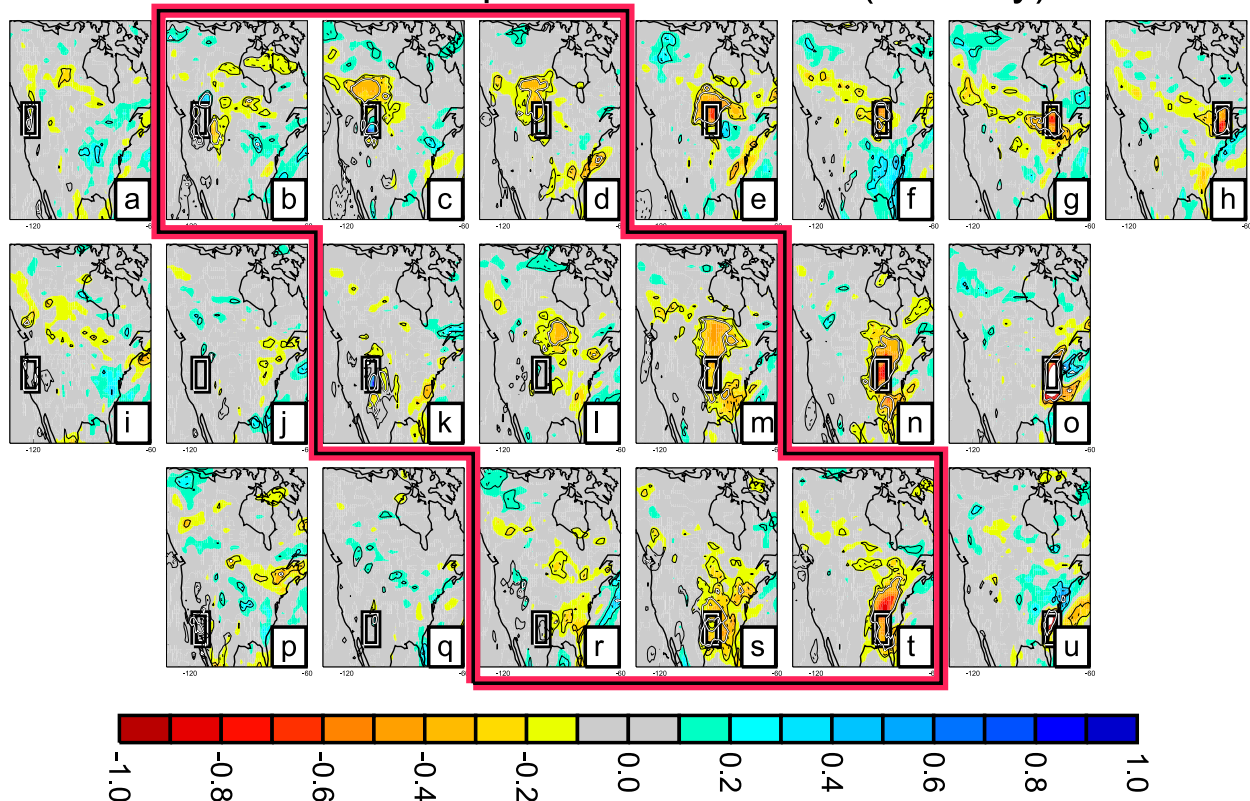## Induced Precipitation Anomalies (mm/day)

FIG. 8. As in Fig. 7, but for precipitation anomalies (mm day^{-1}).

c. Signals inherent in observations-based data

The results in section 3b relate to the AGCM's inherent climate. While the hope is that they also represent nature, this is, of course, far from guaranteed. Unfortunately, definitively verifying our results with observations is made impossible by the limited extent of available observations-based data. To a large extent the shifts examined in the experiments above are subtle; given the large number of simulations constituting our ensembles, we are effectively examining here the net impact of shifts in probability distribution functions (PDFs). Reanalyses, which typically cover less than 40 years, are inadequate for a proper analysis of PDF shifts. Another key difficulty is the fact that when soil moisture in nature is dry in, say, region K of Fig. 2, it also tends to be anomalously dry elsewhere (say, in regions L and M), complicating tremendously the isolation of specific impacts associated with region K's dryness.

The analyses above, however, suggest a way of addressing at least the second difficulty. Despite the spatial shifts in the local diabatic heating induced by the different dryness regions in Fig. 2, the atmosphere in the different SWM and AGCM experiments responds in a similar way: dry conditions (or diabatic atmospheric heating associated with dry conditions) in the interior of the United States tend to produce a similar streamfunction anomaly pattern. A possible inference from this result is that in the complex set of available observations, the key feature to look for is not a soil moisture deficit in a specific region but an average dryness in a large continental region (viz., that delimited in Fig. 4a), without regard to the spatial distribution of this dryness—where it is maximized, where it is small, etc. If the SWM and AGCM results are valid, then the atmosphere should tend to show the same response to overall continental dryness regardless of the specific spatial pattern.

With this in mind, we now analyze observations-based 250-hPa streamfunction, precipitation, and air temperature fields associated with continental-scale antecedent land surface dryness.

1) COMPOSITING STRATEGY

We use a compositing approach to draw out signals, if they exist, in the observations-based data. Within each year of 1980–2014, we consider six 10-day periods: 1–10, 11–20, and 21–30 June and 1–10, 11–20, and 21–30 July,

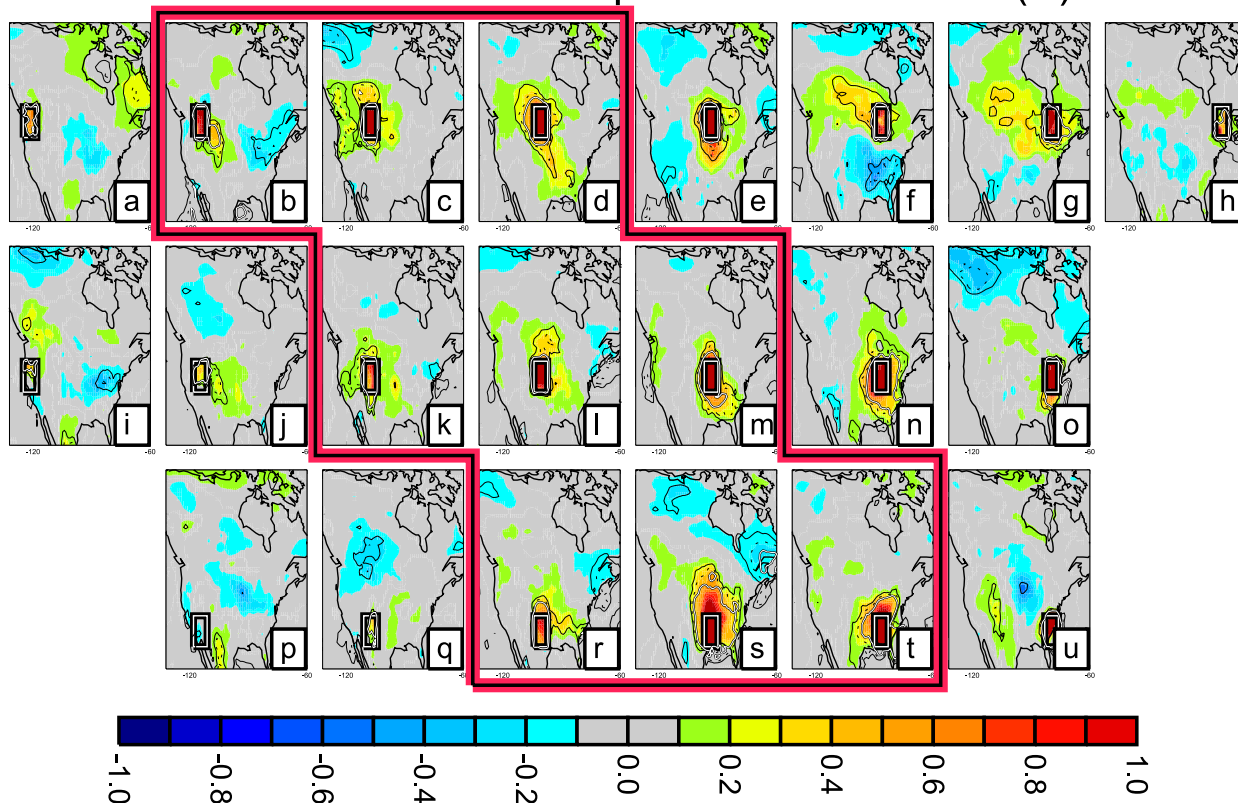## Induced 2-m Air Temperature Anomalies (K)

FIG. 9. As in Fig. 7, but for 2-m air temperature anomalies (K).

amounting to a total of 210 ten-day periods. We tie to each period an antecedent soil moisture index in the following way. First, we standardize, on a daily basis, the MERRA-2 root zone soil moisture within each grid cell of the interior region demarcated in Fig. 4a. Then, for the 10-day period in question, we identify the date falling 15 days prior to the start of the period and compute, for that day, the average of the standardized soil moisture values across the region. A large negative value for this average implies that, on average, the large-scale continental region was generally very dry 15 days prior to the period in question. (See section 2c for a discussion of the realism of MERRA-2 soil moisture values.) We use soil moistures at a 15-day lead rather than concurrent soil moistures to help ensure that the soil moisture signals on which we base our composites are not simply a passive reflection of the meteorology we are examining. Fifteen days lies above the typical time scales of planetary wave development and maintenance in response to local heating anomalies.

Our composites are based on the driest 10% of antecedent average soil moisture values. From the 210 June–July decads examined, we thus compute the average

250-hPa streamfunction, precipitation, and air temperature anomaly fields over the 21 driest cases.

2) RESULTS

Figures 10a–c show respectively the resulting composites of 250-hPa streamfunction (from ERA-Interim), precipitation (from CPCU, via MERRA-2), and 2-m air temperature (from ERA-Interim). The composited full streamfunction field shows a high along the U.S.–Canadian border in the central part of the continent. The composited precipitation field shows a reduction of precipitation along the eastern border of the demarcated interior region along with some increases in precipitation in various surrounding areas, and the composited temperature field shows a positive temperature anomaly that spans much of the interior region.

For comparison, Fig. 10d shows the corresponding streamfunction anomaly field from the SWM experiments; it shows the sum of the fields obtained in the experiments imposing diabatic heating anomalies within the indicated region. The positioning of the positive streamfunction lobe from the observational composite agrees to a first order with that in the SWM results. While the
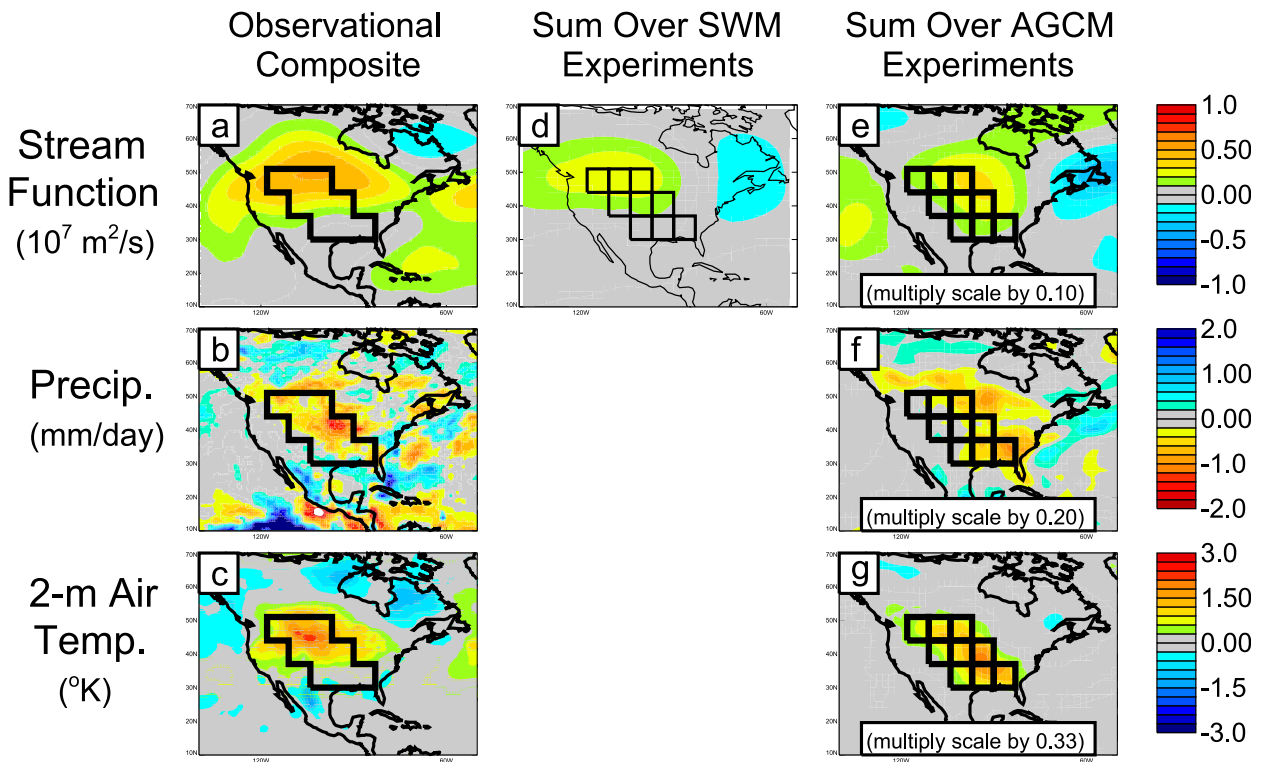
FIG. 10. (a) Composited field of 250-hPa streamfunction anomalies from ERA-Interim, built from the 10% of the 210 June and July decads during 1980–2014 with the driest antecedent (15-day lead) continental soil moistures in the region indicated. (b) As in (a), but for MERRA-2 rain gauge corrected precipitation. (c) As in (a), but for ERA-Interim 2-m air temperatures. (d) Average of the June–July 250-hPa eddy streamfunction anomalies produced in the nine SWM experiments indicated. (e) Sum of the June–July 250-hPa streamfunction anomalies produced in the nine AGCM experiments indicated. (f) As in (e), but for precipitation. (g) As in (e), but for 2-m air temperature.

observational composite is largely missing the negative lobe in the east, the square of the spatial correlation coefficient between the patterns in Figs. 10a and 10d over the full area of each panel is reasonably high ($r^2 = 0.36$).

Finally, Figs. 10e–g show the corresponding fields derived from the AGCM experiments. To construct the figures, we simply add together the June–July anomalies of the experiments corresponding to the areas delimited by the thick black lines, making the assumption (as we did above for the SWM) that, in the AGCM, the effects of the different dryness areas on continental meteorology combine linearly. [This assumption is strongly supported by the results of Koster et al. (2014, their Fig. 5).] In comparing the observational composites and the AGCM results, the first thing to note is the difference in scale. This said, notice that the patterns inherent in the observational composites and the AGCM results are again similar. Only slight spatial shifts, for example, are seen in the positions of the large precipitation and air temperature anomalies.

We emphasize here that these results do not prove that the SWM and AGCM experiments properly represent

nature. Again, the experiments address the net impact of shifts in the underlying PDFs of the meteorological fields, shifts that cannot be captured by the limited observational record. That is, even if the model results represented nature perfectly (which, given their inherent biases, they presumably do not), we would still expect to see differences between the observational and model results. Nevertheless, the comparisons in Fig. 10 are promising; they show that the experimental results are at least consistent with available observations.

d. Additional findings regarding remote land surface impacts

The similarity in the pattern of the atmospheric response to dryness in different parts of the North American continent is the main result of this study. Nevertheless, the AGCM experiments hold a wealth of information that can be tapped for further understanding of land–atmosphere interactions. Here, we distill the extensive amount of information in Figs. 7–9 into two simple aggregate quantities, quantities that together characterize the first-order impact of soil moisture

anomalies on meteorological variables in remote locations and how this impact varies with location.

The first aggregate quantity, the "impact extent," measures the spatial extent of the impact of each imposed dryness region in Fig. 2. While it is related in concept to more sophisticated diagnostics described in the literature for characterizing the remote reach of localized anomalies [e.g., the climate sensitivity maps constructed by Barsugli et al. (2006) from the results of SST warm patch experiments], the diagnostic we use here is more limited, focusing only on the spatial extent of this reach rather than on the amplitude of the response. Our quantity is computed as follows. For a given experiment, and for a given meteorological variable (precipitation or air temperature), we count the number of $1° \times 1°$ grid cells in North America (at least the part of North America shown in Fig. 11) for which the change in the meteorological variable determined for the experiment was significantly different from zero at the 99% confidence level or higher, according to a Student's t test. This number, which indeed reflects the area within the dashed contours in Figs. 8 and 9, is then plotted in Fig. 11—the number computed for a given experiment is plotted within the corresponding imposed dryness area for that experiment.

Figure 11a shows that for precipitation, the impact extent is highest for the dryness regions encompassing the Gulf Coast and parts of the Mississippi River valley (regions M, N, S, and T). When these areas are forced to be dry, the remote (plus local) impacts of the dryness are felt across a relatively large area. High values also appear in an area around Montana (regions B and C). Values along either coast are relatively small, meaning that when these areas are dry the spatial extent of the resulting impact on precipitation is slight. In fact, as might be expected, the impact extent varies to some degree with the impact of the drying on the June–July evaporation rates (Fig. 5b). (Note that a 99% confidence level suggests that roughly 1%, or 36 of the 3621 grid cells considered here, will be falsely labeled significant. Values below 48 in the plots are shaded gray, suggesting little or no impact.)

For air temperature (Fig. 11b), region S has the greatest impact extent, followed by region B. Aside from region O, dryness regions along either coast again have minimal or no impact. Curiously, for some experiments, spatial impacts on air temperature appear smaller than those on precipitation, despite the fact that for air temperature a local impact at the very least is almost guaranteed due to a reduction in local evaporative cooling.

The second aggregate quantity, the "sensitivity to remote dryness," measures the degree to which a given grid cell is affected by soil moisture anomalies in different regions. This sensitivity is computed at each grid cell as the number of different experiments for which a meteorological quantity (precipitation or air temperature) at the grid cell was modified at a significance level of 99% or higher, according to a Student's t test. Figure 12a shows the spatial distribution of the sensitivity for precipitation. Notice that 4–6 distinct dryness areas are able to affect the June–July precipitation in various grid cells along the eastern half of the U.S.–Canadian border; by this measure, these grid cells are particularly susceptible to remote effects. In general, the eastern half of the United States is more sensitive to U.S. soil moisture dryness than the western half. The corresponding plot for air temperature (Fig. 12b) also shows an east–west contrast but locates the region of highest sensitivity to remote dryness along the southeastern coast. Of course, it is important to keep in mind that the patterns in Fig. 12 are determined, to some degree, by the distribution of dryness regions in Fig. 2. If we had examined additional experiments with imposed dryness in Canada and Mexico, the patterns in Fig. 12 would presumably be modified, particularly in or near these outside regions.

The quantities plotted in Figs. 11 and 12 are, in some ways, converses of each other; Fig. 11 in essence shows the strength (local plus remote) of a "source" of meteorological anomalies, and Fig. 12 shows, in a way, the strength of their "sink." The locations of the sources and sinks are different, underlining the geographical connections that exist between land areas through the overlying circulation and its sensitivity to surface processes.

4. Summary and discussion

The simulations with the stationary wave model (SWM) suggest that when a diabatic heating anomaly is imposed in the interior of the continental United States (anywhere within the delimited area in Fig. 4a) during boreal summer, the atmospheric circulation responds in a very similar way: it produces a positive eddy streamfunction anomaly in the west-central part of the continent and a negative anomaly to the east. This basic response is also seen, at least to a first order, in AGCM experiments when soil moisture contents in different parts of the continental interior are forced to be dry. The AGCM experiments further allow us to identify impacts of the imposed soil moisture dryness on remote near-surface meteorological fields. As indicated by the averages in the right-hand column of Fig. 10, dry soil moistures in the interior continental region tend to produce warm conditions within the region (Fig. 10g)

a. Prec: # cells affected at 99% confidence level by source
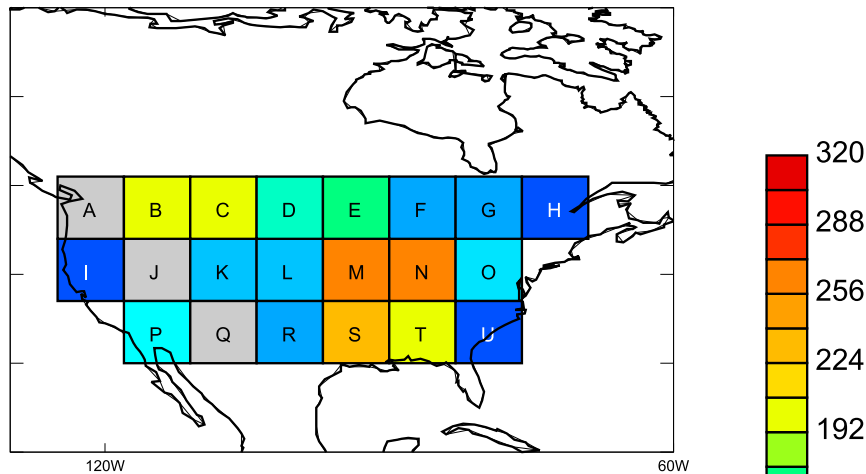
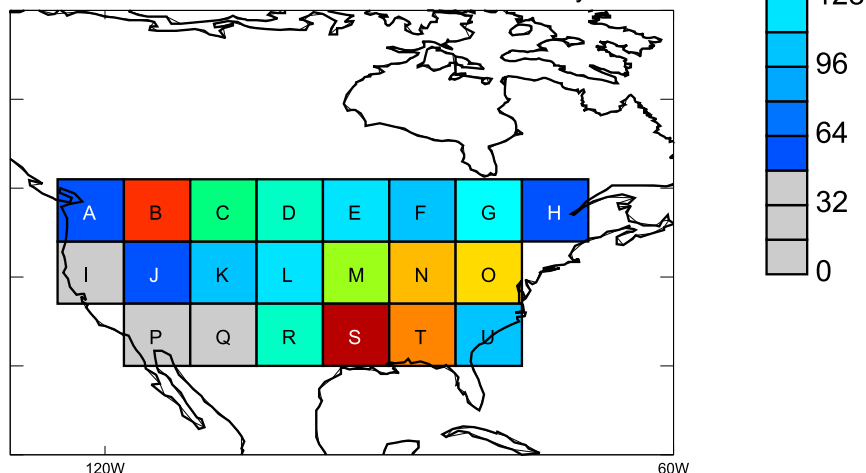b. T2m: # cells affected at 99% confidence level by source

FIG. 11. (a) Number of 1° × 1° grid cells across the indicated region (20°–70°N, 130°–60°W) for which precipitation is modified at the 99% confidence interval by the dryness imposed in each experiment. (The number of grid cells affected in a given experiment is shaded in color within the dryness region associated with that experiment.) Gray shading indicates very roughly the number expected by chance. (b) As in (a), but for 2-m air temperature.

and reduced rainfall a little to the east (Fig. 10f). Observational composites (Figs. 10a–c) are consistent, again to a first order, with the modeled impacts. (It is worth emphasizing again that all of these results are for June–July only; land dryness impacts may be reduced during nonsummer months due to reductions in surface turbulent fluxes associated with reduced solar forcing.)

The overall behavior established in our experiments is strongly suggestive of a positive feedback loop, as captured in the schematic in Fig. 13: dry conditions within the continental interior lead to changes in the atmospheric circulation that in turn lead to further warming and drying there. Consider, for example, the results of

imposing soil moisture dryness in region L of Fig. 1. According to Fig. 7l, this leads to a 250-hPa streamfunction high over region L that also extends farther to the north. Figures 8l and 9l show that this in turn leads to a warm and dry anomaly just north of the region—conditions that, according to experiment AGCM-D, should lead to additional warming and drying in the area (Figs. 8d and 9d). The positive feedback loop outlined in Fig. 13 may have impacts on the spatial extent of drought, helping a local dry anomaly in, say, Kansas and Nebraska spread spatially across the continental interior. The mechanics of this feedback loop are worthy of further study.
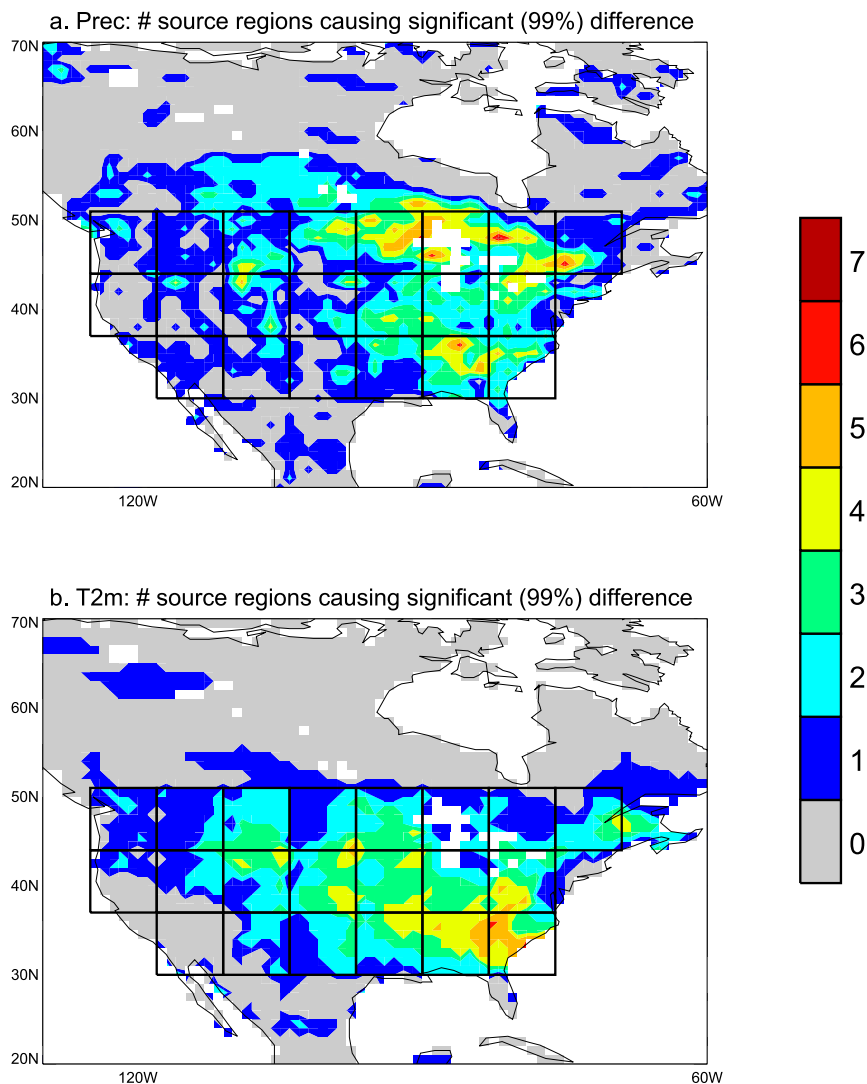
a. Prec: # source regions causing significant (99%) difference

b. T2m: # source regions causing significant (99%) difference

FIG. 12. (a) For each $1° \times 1°$ grid cell, the number of dryness regions (as outlined in the thick black lines) that, in our experiments, induce precipitation anomalies significant at the 99% confidence level. (b) As in (a), but for 2-m air temperature.

What are the mechanisms by which an atmospheric circulation anomaly translates to anomalies in surface air temperature and precipitation? At these latitudes, streamfunction anomalies and geopotential height anomalies are largely coincident, and as discussed in Koster et al. (2014), an upper-level positive height anomaly can affect surface temperature through an associated increase in subsidence, which promotes cloudless skies and thereby an increased amount of incoming solar radiation reaching the surface. Lower-level circulation changes, however, are undoubtedly also important, as they can lead to precipitation anomalies through changing atmospheric moisture transport and convergence in the lower troposphere. We should note that the lower-level impacts among the experiments are less

systematic. Anomalies in 850-hPa wind circulation patterns (not shown), as generated by the different AGCM experiments, do not show the level of agreement seen in Fig. 7, largely because the anomalies are of smaller spatial extent and tend to be more centered over the individual imposed dryness regions. This said, however, some agreement in the 850-hPa wind response is seen, and supplemental analyses of the AGCM results indicate that the west-central North America streamfunction anomaly produced in most of our experiments does tend to tilt westward with height. This westward tilt may explain why the precipitation anomalies produced in our AGCM experiments tend to lie slightly eastward of the air temperature anomalies (cf. Figs. 10f and 10g), given that precipitation deficits are largely maintained
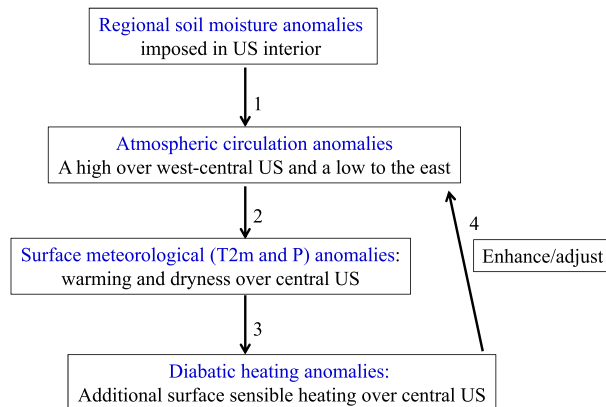
FIG. 13. Schematic of a potential feedback loop suggested by the AGCM results. The dry soil moisture induces 1) a specific circulation pattern that in turn induces 2) additional warming and drying over the central United States. This in turn leads to 3) higher sensible heat fluxes from the land surface in the central United States, which can enhance 4) the atmospheric circulation anomaly that originally produced the warming and drying.

by reduced atmospheric moisture flux convergences due to changes in low-level atmospheric circulation (e.g., Wang et al. 2010; Wang and Schubert 2014). Meanwhile, changes in low-level winds bring, in some cases, warm air in from the south, further increasing temperature (not shown). A full understanding of the mechanisms linking the 3D circulation patterns to surface anomalies needs additional study through focused experimentation and associated budget analysis for surface energy, air temperature, and atmospheric moisture.

While the feedback loop outlined in Fig. 13 is intriguing, we must emphasize again a critical aspect of our results, namely, the need for large ensembles (96–192 members) to draw out the indicated patterns in Figs. 7–9. The size of these ensembles speaks to the weakness of the model atmosphere's response to the imposed surface anomalies; as noted above, our experiments effectively address shifts in the PDFs of atmospheric response. Dry conditions for a given year in the central United States will not necessarily lead to the indicated streamfunction anomalies during that year and an associated strengthening of the dry anomaly; all we can claim is an increased likelihood for this to happen.

In other words, the feedback's operation in the AGCM is probabilistic. It is presumably probabilistic in nature as well. The fact that the magnitudes of the responses in Fig. 10 are larger for the observational composites than for the model results (while the patterns are roughly the same) in fact may suggest that the feedback in the model is weaker than it is in nature. Additional work is needed to learn if this is true and whether the feedback is indeed large enough in nature to be useful for, say, forecast applications.

Perhaps most intriguing of all is our finding, through both the SWM and AGCM analyses, that the atmospheric circulation responds in such a consistent way to surface heating anomalies regardless of the specific geographical positioning of these anomalies within the continental interior (Figs. 3 and 7). We are currently performing analyses aimed at explaining this marked similarity in response and the relatively reduced response produced when the dry anomalies are near the western or eastern coast.

REFERENCES

Adler, R. F., and Coauthors, 2003: The version-2 Global Precipitation Climatology Project (GPCP) monthly precipitation analysis (1979–present). *J. Hydrometeor.*, **4**, 1147–1167, doi:10.1175/1525-7541(2003)004<1147:TVGPCP>2.0.CO;2.

Bacmeister, J. T., M. J. Suarez, and F. R. Robertson, 2006: Rain reevaporation, boundary layer convection interactions, and Pacific rainfall patterns in an AGCM. *J. Atmos. Sci.*, **63**, 3383–3403, doi:10.1175/JAS3791.1.

Barsugli, J. J., S.-I. Shin, and P. D. Sardeshmukh, 2006: Sensitivity of global warming to the pattern of tropical ocean warming. *Climate Dyn.*, **27**, 483–492, doi:10.1007/s00382-006-0143-7.

Betts, A. K., and J. H. Ball, 1995: The FIFE surface diurnal cycle climate. *J. Geophys. Res.*, **100**, 25 679–25 693, doi:10.1029/94JD03121.

——, ——, A. C. M. Beljaars, M. J. Miller, and P. Viterbo, 1994: Coupling between land-surface, boundary-layer parameterizations and rainfall on local and regional scales: Lessons from the wet summer of 1993. Preprints, *Fifth Conf. on Global Change Studies*, Nashville, TN, Amer. Meteor. Soc., 174–181.

Bosilovich, M., and Coauthors, 2015: MERRA-2: Initial evaluation of the climate. NASA/TM-2012-104606, Vol. 43, 139 pp.

Chou, M.-D., 1990: Parameterizations for the absorption of solar radiation by O_2 and CO_2 with applications to climate studies. *J. Climate*, **3**, 209–217, doi:10.1175/1520-0442(1990)003<0209:PFTAOS>2.0.CO;2.

——, 1992: A solar radiation model for use in climate studies. *J. Atmos. Sci.*, **49**, 762–772, doi:10.1175/1520-0469(1992)049<0762:ASRMFU>2.0.CO;2.

——, and M. J. Suarez, 1994: An efficient thermal infrared radiation parameterization for use in general circulation models. NASA Tech. Memo. 104606, Vol. 3, 84 pp.

Cohen, J., J. C. Furtado, J. Jones, M. Barlow, D. Whittleston, and D. Entekhabi, 2014: Linking Siberian snow cover to precursors of stratospheric variability. *J. Climate*, **27**, 5422–5432, doi:10.1175/JCLI-D-13-00779.1.

Dee, D. P., and Coauthors, 2011: The ERA-Interim reanalysis: Configuration and performance of the data assimilation

system. *Quart. J. Roy. Meteor. Soc.*, **137**, 553–597, doi:10.1002/qj.828.

Delworth, T. L., and S. Manabe, 1989: The influence of soil wetness on near-surface atmospheric variability. *J. Climate*, **2**, 1447–1462, doi:10.1175/1520-0442(1989)002<1447:TIOSWO>2.0.CO;2.

Dirmeyer, P. A., S. Kumar, M. J. Fennessy, E. L. Altshuler, T. DelSole, Z. C. Guo, B. A. Cash, and D. Straus, 2013: Model estimates of land-driven predictability in a changing climate from CCSM4. *J. Climate*, **26**, 8495–8512, doi:10.1175/JCLI-D-13-00029.1.

Douville, H., 2002: Influence of soil moisture on the Asian and African monsoons. Part II: Interannual variability. *J. Climate*, **15**, 701–720, doi:10.1175/1520-0442(2002)015<0701:IOSMOT>2.0.CO;2.

——, and F. Chauvin, 2000: Relevance of soil moisture for seasonal climate predictions: A preliminary study. *Climate Dyn.*, **16**, 719–736, doi:10.1007/s003820000080.

Entin, J. K., A. Robock, K. Y. Vinnikov, S. E. Hollinger, S. Liu, and A. Namkhai, 2000: Temporal and spatial scales of observed soil moisture variations in the extratropics. *J. Geophys. Res.*, **105**, 11 865–11 877, doi:10.1029/2000JD900051.

Findell, K. L., and E. A. B. Eltahir, 1997: An analysis of the soil moisture–rainfall feedback, based on direct observations from Illinois. *Water Resour. Res.*, **33**, 725–735, doi:10.1029/96WR03756.

Gates, W. L., 1992: AMIP: The Atmospheric Model Intercomparison Project. *Bull. Amer. Meteor. Soc.*, **73**, 1962–1970, doi:10.1175/1520-0477(1992)073<1962:ATAMIP>2.0.CO;2.

Gelaro, R., and Coauthors, 2014: Evaluation of the 7-km GEOS-5 Nature Run. NASA/TM-2014-104606, Vol. 36, 285 pp. [Available online at http://ntrs.nasa.gov/search.jsp?R=20150011486.]

Guo, Z., and Coauthors, 2006: GLACE: The Global Land–Atmosphere Coupling Experiment. Part II: Analysis. *J. Hydrometeor.*, **7**, 611–625, doi:10.1175/JHM511.1.

Ham, Y.-G., S. D. Schubert, Y. Vikhliaev, and M. J. Suarez, 2014: An assessment of the ENSO forecast skill of the GEOS-5 system. *Climate Dyn.*, **43**, 2415–2430, doi:10.1007/s00382-014-2063-2.

Held, I. M., M. Ting, and H. Wang, 2002: Northern winter stationary waves: Theory and modeling. *J. Climate*, **15**, 2125–2144, doi:10.1175/1520-0442(2002)015<2125:NWSWTA>2.0.CO;2.

Helfand, H. M., and S. D. Schubert, 1995: Climatology of the simulated Great Plains low-level jet and its contribution to the continental moisture budget of the United States. *J. Climate*, **8**, 784–806, doi:10.1175/1520-0442(1995)008<0784:COTSGP>2.0.CO;2.

Huffman, G. J., R. F. Adler, D. T. Bolvin, and G. Gu, 2009: Improving the global precipitation record: GPCP version 2.1. *Geophys. Res. Lett.*, **36**, L17808, doi:10.1029/2009GL040000.

Koster, R. D., M. J. Suarez, A. Ducharne, M. Stieglitz, and P. Kumar, 2000: A catchment-based approach to modeling land surface processes in a general circulation model: 1. Model structure. *J. Geophys. Res.*, **105**, 24 809–24 822, doi:10.1029/2000JD900327.

——, ——, R. W. Higgins, and H. M. Van den Dool, 2003: Observational evidence that soil moisture variations affect precipitation. *Geophys. Res. Lett.*, **30**, 1241, doi:10.1029/2002GL016571.

——, and Coauthors, 2006: GLACE: The Global Land–Atmosphere Coupling Experiment. Part I: Overview. *J. Hydrometeor.*, **7**, 590–610, doi:10.1175/JHM510.1.

——, Z. Guo, R. Yang, P. A. Dirmeyer, K. Mitchell, and M. J. Puma, 2009: On the nature of soil moisture in land surface models. *J. Climate*, **22**, 4322–4335, doi:10.1175/2009JCLI2832.1.

——, and Coauthors, 2011: The second phase of the Global Land–Atmosphere Coupling Experiment: Soil moisture contributions to subseasonal forecast skill. *J. Hydrometeor.*, **12**, 805–822, doi:10.1175/2011JHM1365.1.

——, Y. Chang, and S. D. Schubert, 2014: A mechanism for land–atmosphere feedback involving planetary wave structures. *J. Climate*, **27**, 9290–9301, doi:10.1175/JCLI-D-14-00315.1.

Lau, W. K. M, and K.-M. Kim, 2012: The 2010 Pakistan flood and Russian heat wave, Teleconnection of hydrometeorological extremes. *J. Hydrometeor.*, **13**, 392–403, doi:10.1175/JHM-D-11-016.1.

Lock, A. P., A. R. Brown, M. R. Bush, G. M. Martin, and R. N. B. Smith, 2000: A new boundary layer mixing scheme. Part I: Scheme description and single-column model tests. *Mon. Wea. Rev.*, **128**, 3187–3199, doi:10.1175/1520-0493(2000)128<3187:ANBLMS>2.0.CO;2.

Molod, A., L. Takacs, M. Suarez, J. Bacmeister, I.-S. Song, and A. Eichmann, 2012: The GEOS-5 atmospheric general circulation model: Mean climate and development from MERRA to Fortuna. NASA/TM-2012-104606, Vol. 28, 115 pp.

Moorthi, S., and M. J. Suarez, 1992: Relaxed Arakawa Schubert: A parameterization of moist convection for general circulation models. *Mon. Wea. Rev.*, **120**, 978–1002, doi:10.1175/1520-0493(1992)120<0978:RASAPO>2.0.CO;2.

National Research Council, 2010: *Assessment of Intraseasonal to Interannual Climate Prediction and Predictability.* National Academies Press, 181 pp.

Peings, Y., H. Douville, R. Alkama, and B. Decharme, 2011: Snow contribution to springtime atmospheric predictability over the second half of the twentieth century. *Climate Dyn.*, **37**, 985–1004, doi:10.1007/s00382-010-0884-1.

Putman, W. M., and S.-J. Lin, 2007: Finite-volume transport on various cubed-sphere grids. *J. Comput. Phys.*, **227**, 55–78, doi:10.1016/j.jcp.2007.07.022.

Reichle, R. H., and Q. Liu, 2014: Observation-corrected precipitation estimates in GEOS-5. NASA/TM-2014-104606, Vol. 35, 18 pp.

Rienecker, M. M., and Coauthors, 2011: MERRA, NASA's Modern-Era Retrospective Analysis for Research and Applications. *J. Climate*, **24**, 3624–3648, doi:10.1175/JCLI-D-11-00015.1.

Robock, A., M. Mu, K. Vinnikov, and D. Robinson, 2003: Land surface conditions over Eurasia and Indian summer monsoon rainfall. *J. Geophys. Res.*, **108**, 4131, doi:10.1029/2002JD002286.

Schubert, S. D., H. Wang, and M. Suarez, 2011: Warm season subseasonal variability and climate extremes in the Northern Hemisphere: The role of stationary Rossby waves. *J. Climate*, **24**, 4773–4792, doi:10.1175/JCLI-D-10-05035.1.

——, ——, R. D. Koster, M. J. Suarez, and P. Ya. Groisman, 2014: Northern Eurasian heat waves and droughts. *J. Climate*, **27**, 3169–3207, doi:10.1175/JCLI-D-13-00360.1.

Seneviratne, S. I., T. Corti, E. L. Davin, M. Hirschi, E. B. Jaeger, I. Lehner, B. Orlowsky, and A. J. Teuling, 2010: Investigating soil moisture–climate interactions in a changing climate: A review. *Earth-Sci. Rev.*, **99**, 125–161, doi:10.1016/j.earscirev.2010.02.004.

Simmons, A. J., K. M. Willett, P. D. Jones, P. W. Thorne, and D. P. Dee, 2010: Low-frequency variations in surface atmospheric humidity, temperature, and precipitation: Inferences from reanalyses and monthly gridded observational data sets. *J. Geophys. Res.*, **115**, D01110, doi:10.1029/2009JD012442.

Taylor, C. M., A. Gounou, F. Guichard, P. P. Harris, R. J. Ellis, F. Couvreux, and M. De Kauwe, 2011: Frequency of Sahelian

storm initiation enhanced over mesoscale soil-moisture patterns. *Nat. Geosci.*, **4**, 430–433, doi:10.1038/ngeo1173.

Thomas, J. A., A. A. Bert, and W. J. Merryfield, 2015: Influence of snow and soil moisture initialization on sub-seasonal predictability and forecast skill in boreal spring. *Climate Dyn.*, **47**, 49–65, doi:10.1007/s00382-015-2821-9.

Ting, M. F., and L. H. Yu, 1998: Steady response to tropical heating in wavy linear and nonlinear baroclinic models. *J. Atmos. Sci.*, **55**, 3565–3582, doi:10.1175/1520-0469(1998)055<3565:SRTTHI>2.0.CO;2.

Vinnikov, K. Ya., and I. B. Yeserkepova, 1991: Soil moisture: Empirical data and model results. *J. Climate*, **4**, 66–79, doi:10.1175/1520-0442(1991)004<0066:SMEDAM>2.0.CO;2.

Wang, A., T. J. Bohn, S. P. Mahanama, R. D. Koster, and D. P. Lettenmaier, 2009: Multimodel ensemble reconstruction of drought over the continental United States. *J. Climate*, **22**, 2694–2712, doi:10.1175/2008JCLI2586.1.

Wang, H., and S. D. Schubert, 2014: The precipitation response over the continental United States to cold tropical Pacific sea surface temperatures. *J. Climate*, **27**, 5036–5055, doi:10.1175/JCLI-D-13-00453.1.

——, ——, M. J. Suarez, and R. D. Koster, 2010: The physical mechanisms by which the leading patterns of SST variability impact U.S. precipitation. *J. Climate*, **23**, 1815–1836, doi:10.1175/2009JCLI3188.1.

——, ——, and R. D. Koster, 2016: North American drought and links to northern Eurasia: The role of stationary Rossby waves. *Climate Extremes: Mechanisms and Potential Prediction, Geophys. Monogr.*, Amer. Geophys. Union, in press.

Xia, Y., and Coauthors, 2012: Continental-scale water and energy flux analysis and validation for the North American Land Data Assimilation System project phase 2 (NLDAS-2): 1. Intercomparison and application of model products. *J. Geophys. Res.*, **117**, D03109, doi:10.1029/2011JD016048.

Xue, Y., R. Vasic, Z. Janjic, Y. M. Liu, and P. C. Chu, 2012: The impact of spring subsurface soil temperature anomaly in the western U.S. on North American summer precipitation: A case study using regional climate model downscaling. *J. Geophys. Res.*, **117**, D11103, doi:10.1029/2012JD017692.